

Paper

Int'l J. of Aeronautical & Space Sci. 16(2), 123–136 (2015)
DOI: <http://dx.doi.org/10.5139/IJASS.2015.16.2.123>

Numerical simulation of jet flow impinging on a shielded Hartmann whistle

Edin Michael*

Department of Mechanical Engineering, College of Engineering Trivandrum, Thiruvananthapuram 695016, India

S. Narayanan**

Department of Mechanical Engineering, Indian School of Mines Dhanbad 826004, India

Abdul Jaleel. H***

Department of Mechanical Engineering, College of Engineering Trivandrum, Thiruvananthapuram 695016, India

Abstract

The present study numerically investigates the effect of shield on the flow characteristics of Hartmann whistle. The flow characteristics of un-shielded Hartmann whistle are compared with whistles of different shield heights 15 mm, 17 mm, 20 mm, 25 mm and 30 mm. The comparison of Mach number contours and transient velocity vectors of shielded Hartmann whistles with un-shielded ones for the same conditions reveal that the presence of shield causes the exiting jet to stick to the wall of the shield without causing spill-over around the cavity inlet, thus sustaining the shock oscillation as seen in the un-shielded Hartmann whistle, which has intense flow/shock oscillation and spill-over around the cavity mouth. The velocity vectors indicate jet regurgitation in shielded whistles showing inflow and outflow phases like un-shielded ones with different regurgitant phases. The sinusoidal variation of mass flow rate at the cavity inlet in un-shielded Hartmann whistle indicates jet regurgitation as the primary operating mode with large flow diversion around the cavity mouth whereas the non-sinusoidal behavior in shielded ones represent that the jet regurgitation is not the dominant operating mode. Thus, this paper sufficiently demonstrates the effect of shield in modifying the flow/shock oscillations in the vicinity of the cavity mouth.

Key words: Hartmann Whistle, Shielding Effect

Nomenclature

D_c	Cavity diameter, m
D_{fej}	Fully expanded jet diameter, m
D_j	Jet exit diameter, m
d	Distance from the jet exit along the x-axis, m
L	Cavity length, m
L_{shock}	Length of the shock-cell, m
M_j	Mach number at the nozzle exit
P_a	Ambient pressure, Pa
P_o	Stagnation pressure, Pa

NPR	Nozzle pressure ratio, (P_o / P_a)
SD	Stand-off distance, m
v_j	Jet velocity at the nozzle exit, m/s
S	Shield height measured from the jet axis, m

1. Introduction

Hartmann whistle is an open-closed cavity for which a high-speed jet strikes at the open end of a cavity that is closed at the other end. The key parameters that control the

This is an Open Access article distributed under the terms of the Creative Commons Attribution Non-Commercial License (<http://creativecommons.org/licenses/by-nc/3.0/>) which permits unrestricted non-commercial use, distribution, and reproduction in any medium, provided the original work is properly cited.

© * Post Graduate Student
** Formerly, Assistant Professor, College of Engineering Trivandrum, Presently, Assistant Professor, Indian School of Mines, Dhanbad, Corresponding author : snarayan.1979@gmail.com
*** Associate Professor, College of Engineering Trivandrum

Received: December 11, 2014 Revised: April 8, 2015 Accepted: April 12, 2015
Copyright © The Korean Society for Aeronautical & Space Sciences

123

<http://ijass.org> pISSN: 2093-274x eISSN: 2093-2480

resonant frequency of the cavity are the shape of the cavity edge, the nozzle pressure ratio, the nozzle to cavity stand-off distance, and the cavity length. The shock-cell structure, Mach disk location, flow/shock oscillations occurring at the cavity mouth, other instabilities in the shear layer, etc., can cause an intense resonance that produces a high-intensity, directional acoustic field. The acoustic field that is generated by the cavity can be used in a number of applications, including enhanced mixing in burners, flow and noise control, combustion process control, dust and aerosol coagulation, liquid mixtures emulsion, etc. For flow control, the nature of the pulsating jet coming out of the Hartmann cavity is the most relevant characteristic. The pulsating jet is generally used to improve the performance of flight vehicles by reducing the drag, delaying stall, suppressing acoustical disturbances and reducing emissions. In fact, there is scarcely any literature that shows the effect of upstream shielding on the flow/shock oscillation characteristics of a Hartmann whistle. Therefore, a detailed numerical simulation is carried out in the present study to predict the flow/shock oscillation characteristics of a Hartmann whistle by shielding the area between the jet exit and the cavity inlet, which is the specific objective of this work. The presence of the shield between the jet exit and the cavity inlet is intended to improve the flow/shock oscillations by eliminating the spillover through the side of the cavity wall. Some of the relevant literature on Hartmann whistles is discussed in this section.

Hartmann [1] discovered a resonance phenomenon while conducting experiments to determine the axial variation of the stagnation pressure distribution in a supersonic jet using a Pitot tube. He observed that the Pitot tube undergoes violent oscillations when placed at certain locations in the shock cell containing zone of the free jet where the stagnation pressure increases as the distance from the nozzle increases. He found that acoustic oscillations are emitted and showed that its wavelength had some relation to the longitudinal dimension of the pitot tube assembly.

Chang *et al.* [2] used the Total Variation Diminishing (TVD) scheme to solve the axisymmetric Euler equations in order to study the Hartmann cavity flow. The generation of shock and expansion waves in the cavity and their interactions with the impinging jet were explained through four chronological phases, including intake, transition to expulsion, expulsion, and transition to intake.

Chang and Lee [3] numerically simulated the flow field in a Hartmann cavity and found that its resonant behavior was primarily dependent on the wavelength of the resonant wave as well as on the cavity length rather than on other parameters, such as the frequency, oscillatory Mach number, and distance

from the oscillatory location to the cavity mouth.

Hamed *et al.* [4] showed the effect of the cavity geometry on the unsteady flow characteristics as well as on the mass flow variations of a whistle. The numerical predictions of the pressure oscillations as well as the sound level spectra for the various cavity geometries revealed that the frequency and amplitude of the pressure oscillations were strongly dependent on the cavity length and stand-off distance. Brun and Boucher [5] found that the cavity generates high intensity sound when the ratio of the cavity diameter to the jet diameter (D_c / D_j) lies between 1.33 and 2.5.

Raman *et al.* [6] showed a good match for the frequencies obtained from experiments and those predicted by the quarter wavelength formula for large cavity lengths. However, a variation could be observed for small cavity lengths. Sreejith *et al.* [7] noticed that for the same cavity length, the resonant frequencies of the cylindrical cavities were lower than those of the conical cavities, and they also observed that the low-frequency modes in the kHz range exhibit an oscillatory behavior with the stand-off distance.

Gregory and Sullivan [8] used Pressure-sensitive paint (PSP) to establish the relationship between the unsteady flow dynamics and the acoustics of the Hartmann cavity. They also investigated the nature of the shock oscillations, the unsteady flow interactions and the directivity of the sound emission. Kastner and Samimy [9] developed a Hartmann cavity by covering a main portion of the area between the jet and cavity to easily establish flow control with a pulsating jet. They also noticed that the stand-off distance was a vital parameter for effective flow control.

Brocher *et al.* [10] used a simplified wave diagram and gas and sound speed diagrams to show how fluctuations start and grow within the resonance tube. They found that the amplitude of the oscillations approaches a limiting value when the jet is fully swallowed by the cavity during the compression phase of the cycle. Narayanan *et al.* [11] showed that the maximum power emitted by a chamfered whistle was twice that of a regular Hartmann whistle. Raman and Srinivasan [12] surveyed the research on Hartmann whistles by outlining the progress made from Hartmann's breakthrough until current applications.

1.1 Objectives of the present work

There is sparse literature that investigates the effect of the shield between the jet exit and the cavity inlet on the flow/shock oscillation characteristics of the Hartmann whistle. Therefore, this paper focuses on understanding the nature of the flow/shock oscillation features of the Hartmann whistle by covering all of the free space between the cavity inlet and

the nozzle exit with a cylindrical shield. Passive control is applied to the direction of the pulsating jet by installing a shield, and the exiting jet is expected to move towards the shield, thus eradicating the spillover. The height of the shield is varied as 15 mm, 17 mm, 20 mm, 25 mm and 30 mm, and the other parameters remained constant in order to understand the effect on the flow/shock oscillation features that occur near the cavity mouth. The jet exit diameter (D_j) and the cavity diameter (D_c) shown in Fig. 1 (a) are kept constant at 7 mm. The following section describes the numerical methodology that was used to predict the flow characteristics of the Hartmann whistle.

2. Numerical methodology

2.1 Governing equations

The axisymmetric governing equations that control the physical phenomenon occurring in the system are as follows.

Continuity equation

$$\frac{\partial \rho}{\partial t} + \frac{1}{r} \frac{\partial}{\partial r} (r \rho u_r) + \frac{\partial}{\partial z} (\rho u_z) = 0 \quad (1)$$

r - momentum

$$\rho \frac{Du_r}{Dt} = F_r - \frac{\partial P}{\partial r} + \frac{\partial}{\partial r} \left[2\mu \frac{\partial u_r}{\partial r} + \lambda \nabla \cdot u \right] + \frac{\partial}{\partial z} \left[\mu \left(\frac{\partial u_r}{\partial z} + \frac{\partial u_z}{\partial r} \right) \right] + \frac{2\mu}{r} \left(\frac{\partial u_r}{\partial r} - \frac{u_r}{r} \right) \quad (2)$$

z - momentum

$$\rho \frac{Du_z}{Dt} = F_z - \frac{\partial P}{\partial z} + \frac{\partial}{\partial z} \left[2\mu \frac{\partial u_z}{\partial z} + \lambda \nabla \cdot u \right] + \frac{1}{r} \frac{\partial}{\partial r} \left[\mu \left(\frac{\partial u_r}{\partial z} + \frac{\partial u_z}{\partial r} \right) \right] \quad (3)$$

where

$$\nabla \cdot u = \frac{\partial u_r}{\partial r} + \frac{\partial u_z}{\partial z} + \frac{u_r}{r} \frac{D}{Dt} = \frac{\partial}{\partial t} + u_r \frac{\partial}{\partial r} + u_z \frac{\partial}{\partial z}$$

Energy equation

$$\frac{1}{r} \frac{\partial}{\partial r} \left(k_r \frac{\partial T}{\partial r} \right) + \frac{\partial}{\partial z} \left(k_z \frac{\partial T}{\partial z} \right) + \varphi = \rho \frac{Dh}{Dt} - \frac{Dp}{Dt} \quad (4)$$

where

$$\varphi = 2\mu \left[\left(\frac{\partial u_r}{\partial r} \right)^2 + \left(\frac{u_r}{r} \right)^2 + \left(\frac{\partial u_z}{\partial z} \right)^2 + \frac{1}{2} \left(\frac{\partial u_r}{\partial z} + \frac{\partial u_z}{\partial r} \right)^2 - \frac{1}{3} (\nabla \cdot u)^2 \right]$$

Equation of state

$$P = \rho RT \quad (5)$$

2.2 Solution procedure

2.2.1 Computational domain and Grid

The physical geometry, computational domain and boundary conditions used to simulate the jet flow impinging on the un-shielded and shielded Hartmann whistle are shown in Figs. 1 (a) and 1 (b). The grid was generated using the GAMBIT software for both the shielded and the un-shielded Hartmann whistles. The computational grids of various mesh sizes for Hartmann whistles without and with the shield are shown in Figs. 2 (a) and 2 (b). The grids were made fine in the regions of the shock-cells and were coarse where there are fewer flow effects for the Hartmann whistle without the shield while fine grids were used throughout the domain for the shielded Hartmann whistles. An unsteady axisymmetric simulation was performed using the FLUENT 6.2 software. The flow was considered to be compressible, and a density-based implicit segregated solver was utilized in the current study. No slip boundary conditions were imposed at the walls. The time step size was taken to be of 10^{-6} seconds in order to capture the flow/shock oscillations and the jet regurgitant cycles. A grid sensitivity study was carried out by varying the number of cells as 1.62×10^5 , 1.75×10^5 and 1.89×10^5 , and the result obtained with 1.75×10^5 cells was found to be almost invariant to further grid refinement and

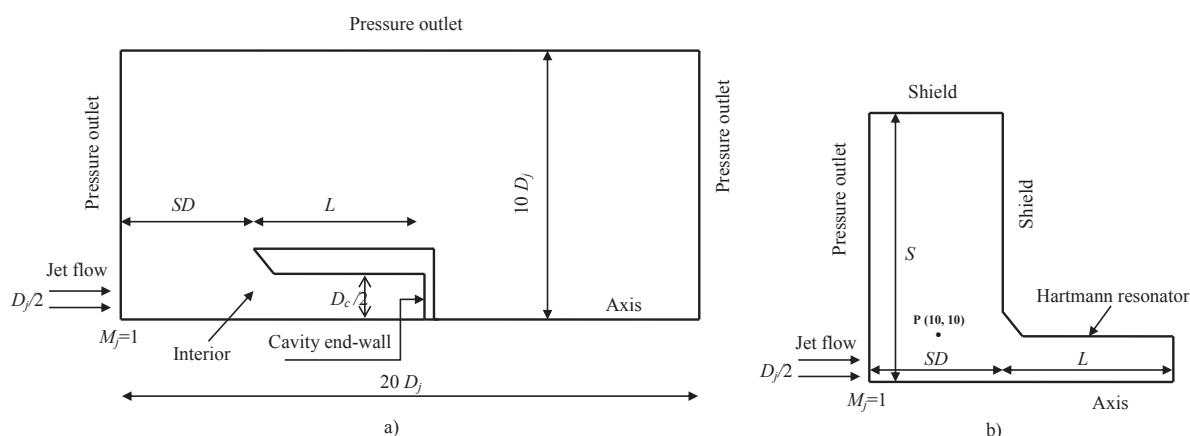


Fig. 1. Computational domain and boundary conditions (a) without shield (WS), (b) with shield

was hence selected for computing all of the different cases.

2.2.2 Turbulence model

The Spalart-Allmaras turbulence model was used to model the turbulence by keeping the standard values of the model constants unchanged ($C_{b1}=0.1355$, $C_{b2}=0.622$, $C_{v1}=7.1$, $\sigma_{\tilde{\nu}}=2/3$, $C_{w1}=3.21$, $C_{w2}=0.3$, $C_{w3}=2.0$, $k=0.4187$). The one equation turbulence model was used to reduce the time required for computation, and it has been seen to provide good results for problems involving wall bounded flows and boundary layers experiencing adverse pressure gradients [13].

The transport variable $\tilde{\nu}$ in the Spalart-Allmaras model is identical to the turbulent kinematic viscosity, except in the viscous-affected near-wall region. The transport equation for $\tilde{\nu}$ is given as

$$\frac{\partial}{\partial t}(\rho\tilde{\nu}) + \frac{\partial}{\partial x_i}(\rho\tilde{\nu}u_i) = G_{\nu} + \frac{1}{\sigma_{\tilde{\nu}}}\left[\frac{\partial}{\partial x_j}(\mu + \rho\tilde{\nu})\frac{\partial\tilde{\nu}}{\partial x_j} + c_{b2}\rho\left(\frac{\partial\tilde{\nu}}{\partial x_j}\right)^2\right] - Y_{\nu} + S_{\tilde{\nu}} \quad (6)$$

where G_{ν} is the production of the turbulent viscosity, and Y_{ν} is the destruction of the turbulent viscosity that occurs in the near-wall region due to wall blocking and viscous damping. $\sigma_{\tilde{\nu}}$ and C_{b2} are constants, and ν is the molecular kinematic viscosity. $S_{\tilde{\nu}}$ is a user-defined source term, and the turbulent viscosity μ_t is computed from $\mu_t = \rho\tilde{\nu}f_{v1}$ where the viscous damping function is $\frac{\chi^3}{\chi^3 + C_{v1}^3}$ and $\chi \equiv \frac{\tilde{\nu}}{\nu}$. The production term G_{ν} is modeled as $G_{\nu} = C_{b1}\rho\hat{S}\tilde{\nu}$, where $\hat{S} \equiv Sc + \frac{\tilde{\nu}}{k^2d^2}f_{v2}$

and $f_{v2} = 1 - \frac{\chi}{1 + \chi f_{v1}}$ where C_{b1} and k are constants, d is the distance from the wall and Sc is a scalar measure of the deformation tensor. The destruction term is modeled as $Y_{\nu} = C_{w1}\rho f_w \left(\frac{\tilde{\nu}}{d}\right)^2$ where $f_w = g\left(\frac{1 + C_{w3}^6}{g^6 + C_{w3}^6}\right)^{1/6}$, and C_{w1} , C_{w2} and C_{w3} are constants.

2.2.3 Validation

In order to ascertain that the numerical predictions were correct, the normalized first shock-cell length (L_{shock}/D_j) for $SD/D_j=2.86$, $L/D_j=4.28$ and $NPR=5$, obtained from the prediction is compared to those determined using Prandtl's expression [14] [Eq. (7)] for a free jet as well as those that were experimentally measured by Narayanan *et al.* [11], as shown in Table 1.

$$L_{shock} = 3.14 \sqrt{\frac{M_j^2 - 1}{2.405}} D_{fej} \quad (7)$$

Tam and Tanna [15] put forth an equation relating the fully expanded jet diameter, D_{fej} , and the exit diameter of the jet, D_j .

$$\frac{D_{fej}}{D_j} = \left\{ \frac{1 + (\gamma - 1)M_j^2/2}{1 + (\gamma - 1)M_d^2/2} \right\}^{\frac{\gamma + 1}{4(\gamma - 1)}} \left(\frac{M_d}{M_j} \right)^{0.5} \quad (8)$$

The fundamental frequency obtained from the current simulation at $SD/D_j=2.86$, $L/D_j=4.28$ and $NPR=5$ for the un-shielded Hartmann whistle also exhibited a good

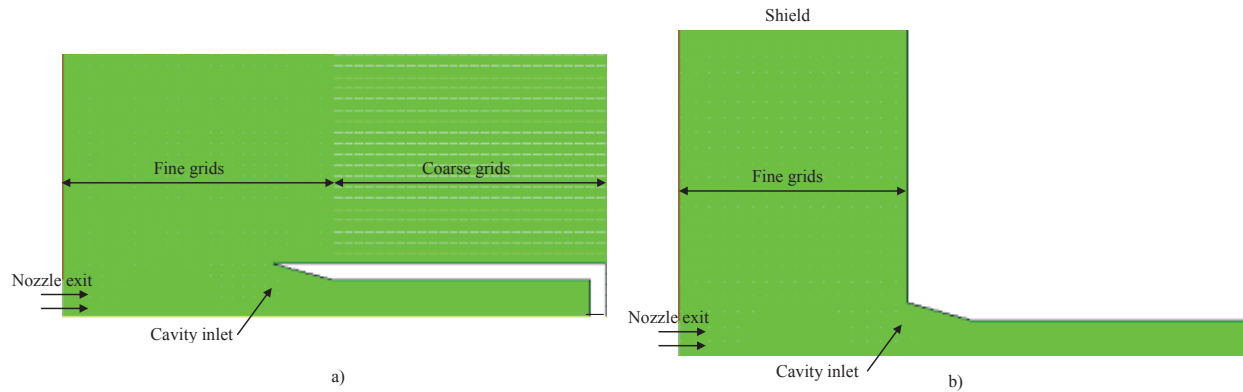


Fig. 2. Grid adopted for Hartmann whistle (a) without shield (WS), (b) with shield

Table 1. Comparison of length of the first shock cell (L_{shock}/D_j)

Length of first shock cell (L_{shock}/D_j) by Narayanan <i>et al.</i> [11]	Length of first shock cell (L_{shock}/D_j) from present computation	Length of first shock cell (L_{shock}/D_j) from theory (Prandtl's expression)
1.83	1.84	2.09

agreement with the corresponding value obtained from the experiments by Narayanan *et al.* [11], as shown in Table 2. A comparisons of the fundamental frequencies obtained from the simulation for various shield heights of the Hartmann whistle (S15, S17, S20, S25 S30) at $SD/D_j=2.86$, $L/D_j=4.28$ and $NPR=5$ are also compared in Table 3.

3. Results and discussion

3.1 Numerical simulation of the flow around a shielded and non-shielded Hartmann whistle

3.1.1 Comparison of the Mach number contours and velocity vectors in the shielded and un-shielded Hartmann whistles.

The Mach number contours and the transient velocity vectors of the Hartmann whistles with a shield height of 17 mm ($S/D_j=2.43$) are compared to those of the un-shielded whistle for the same set of parameters and for relative time instances, as shown in Figs. 3 and 4. By using a shield to cover the region between the whistle and the jet inlet, the exiting jet is seen to stick to the wall of the shield without causing a spill-over around the cavity mouth, thus maintaining a shock oscillation and jet regurgitance, as

Table 2. Comparison of fundamental frequency obtained from experiments and simulation at $SD/D_j=2.86$, $L/D_j=4.28$ and $NPR=5$ for un-shielded and shielded Hartmann whistles

Fundamental frequency obtained for un-shielded Hartmann whistle from experiments by Narayanan <i>et al.</i> [11], kHz	Frequency obtained from simulation, kHz	% deviation
2.23	2.02	9.41

Table 3. Comparison of fundamental frequency obtained from simulation at $SD/D_j=2.86$, $L/D_j=4.28$ and $NPR=5$ for shielded Hartmann whistles

Hartmann whistles with different shield heights, mm	Fundamental frequency obtained from simulation for shielded Hartmann whistles, kHz
15	1.40
17	1.71
20	1.90
25	1.92
30	1.92

seen in the un-shielded Hartmann whistle, which has an intense flow/shock oscillation and spill-over features near the mouth, as already reported by Narayanan *et al.* [11]. The velocity vectors of the shielded Hartmann whistle [Fig. 4 (a)] show an outflow phase whereas the un-shielded whistle shows an inflow phase for the same relative time instances. As the time increases, the strength of the outflow and inflow phases in the shielded and un-shielded Hartmann whistles increase, as shown in Fig. 4 (b). Furthermore, as time increases, the beginning of inflow and outflow phases is

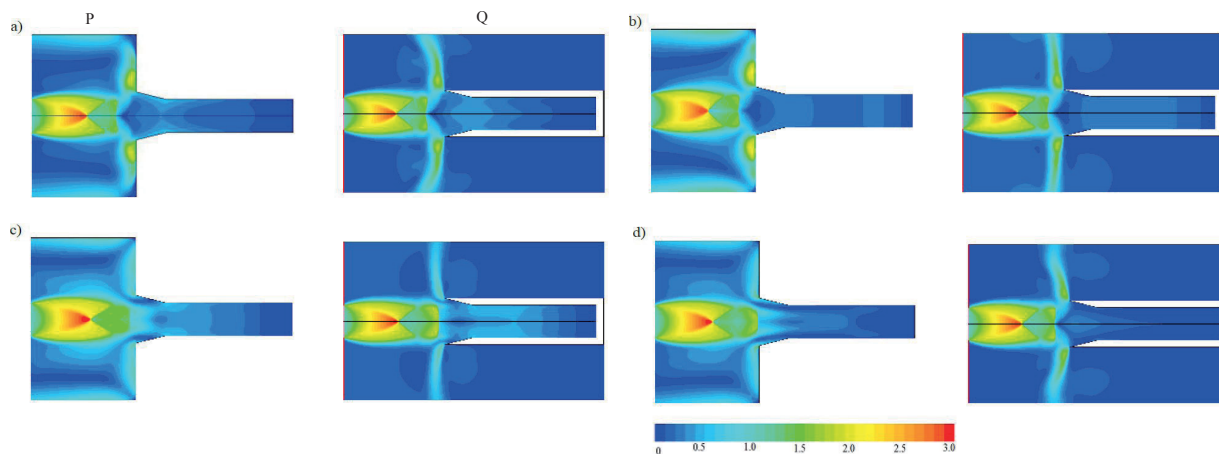


Fig. 3. Comparison of Mach number contours, (P) with $S/D_j=2.43$, (Q) without shield at $\Phi=15^\circ$, $L/D_j=4.28$, $SD/D_j=2.86$, $NPR=5$, at different relative times of (a) $70\mu s$, (b) $210\mu s$, (c) $361\mu s$, (d) $524\mu s$

shown in shielded and un-shielded whistles [Fig. 4 (c)]. The end of the inflow in the shielded whistle and the outflow that gains strength are shown in Fig. 4 (d). Even though the shielded Hartmann whistle exhibits jet regurgitation, as un-shielded ones do, they possess different jet regurgitant phases (i.e., inflow, outflow) at the same relative time instances. The Mach number contours for an increase in shield height of 20 mm ($S/D_j=2.86$), as shown in Figs. 5 (a-d), also exhibit flow/shock oscillations in both the shielded and un-shielded whistles, attachment of the jet to the shield by confiscating the spillover in the shielded whistle, a strong spillover in the un-shielded whistle, etc., all of which are similar to the case mentioned earlier in Fig. 3. The velocity vectors of the shielded whistle represent the outflow phase while the un-shielded whistle shows the end of the outflow phase [Fig. 6 (a)] for the same relative time instances. The end of the outflow phase and the beginning of the inflow phase in the shielded and un-shielded whistles is shown in

Fig. 6 (b). The increase in the strength of the inflow phases for the shielded and un-shielded whistles is shown in Fig. 6 (c). Finally, the beginning of the outflow for both the shielded and un-shielded Hartmann whistles is presented in Fig. 6 (d). The further increase in the shield height to 25 and 30 mm ($S/D_j=3.57, 4.28$) also shows unique features, such as flow/shock oscillations near the cavity mouth in both the shielded and un-shielded Hartmann whistles, attachment of jet to the wall in the shielded whistle that thus eliminates the spill-over, and intense flow diversion in the unshielded Hartmann whistle as seen in the Mach number contours [Figs. 7 (a-d) and 9 (a-d)]. For larger shield heights, the flow/shock oscillations that occur near the mouth of the shielded cavities may be similar to those of the un-shielded ones without a spill-over. The exiting jet sticks to the shield wall, which is a unique characteristic of shielded cavities that prevents external spill-over and also modifies the flow characteristics of the pulsating jet.

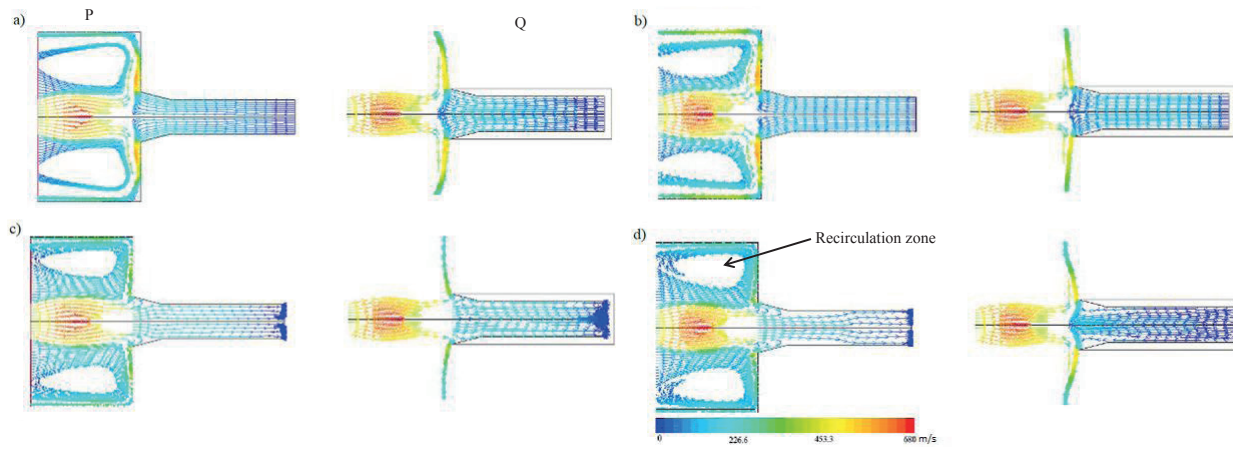


Fig. 4. Comparison of transient velocity vectors, (P) with $S/D_j=2.43$, (Q) without shield at $\Phi=15^\circ$, $L/D_j=4.28$, $S/D_j=2.86$, $NPR=5$, at different relative times of (a) $70\mu s$, (b) $210\mu s$, (c) $361\mu s$, (d) $524\mu s$

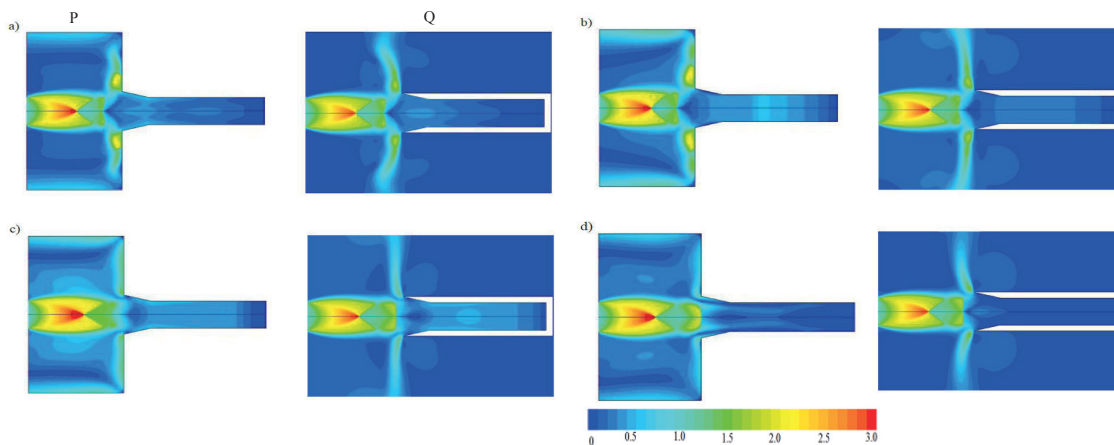


Fig. 5. Comparison of Mach number contours, (P) with $S/D_j=2.86$, (Q) without shield at $\Phi=15^\circ$, $L/D_j=4.28$, $S/D_j=2.86$, $NPR=5$, at different relative times of (a) $58\mu s$, (b) $215\mu s$, (c) $319\mu s$, (d) $497\mu s$

Another unique characteristic that was observed in the shielded cavities is the formation of a recirculation zone

and the achievement of flow control using the pulsating jet. The maximum Mach number for all cases of shielded

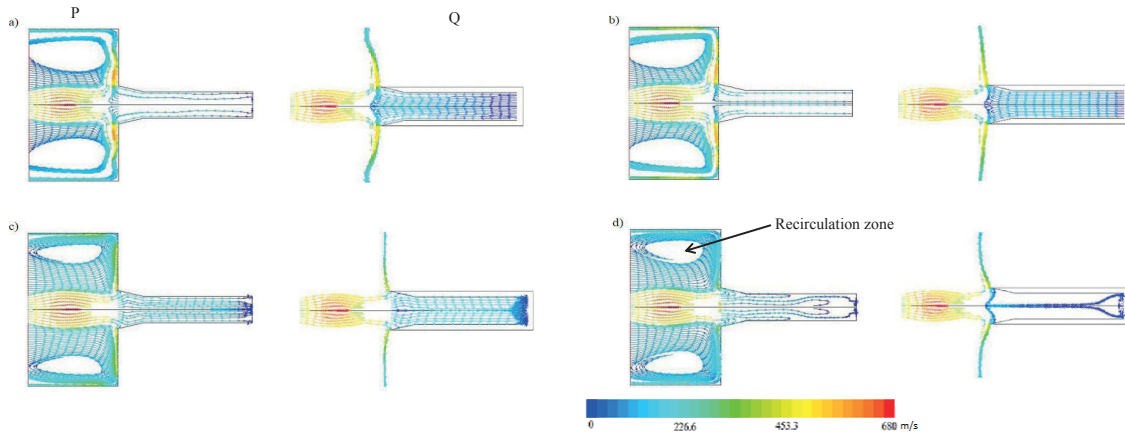


Fig. 6. Comparison of transient velocity vectors, (P) with $S/D_j=2.86$, (Q) without shield at $\Phi=15^\circ$, $L/D_j=4.28$, $S/D_j=2.86$, $NPR=5$, at different relative times of (a) $58\mu s$, (b) $215\mu s$, (c) $319\mu s$, (d) $497\mu s$

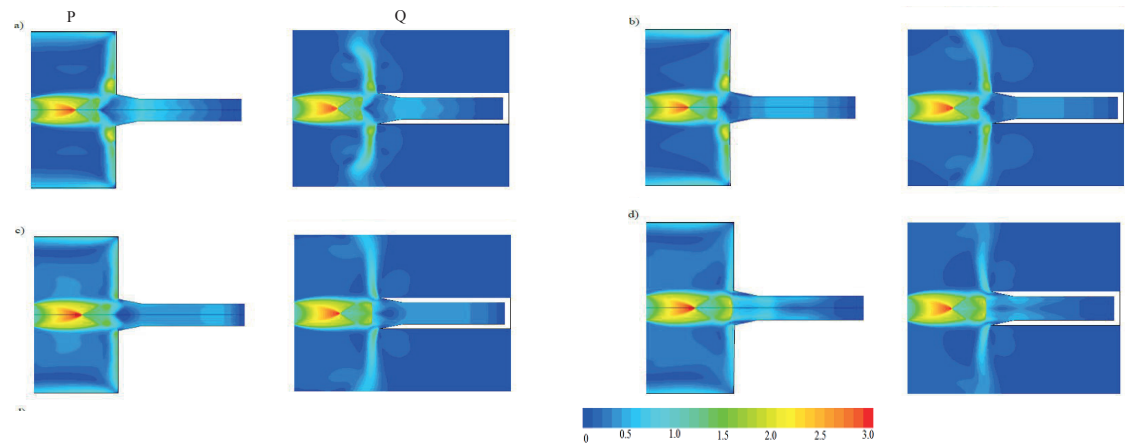


Fig. 7. Comparison of Mach number contours, (P) with $S/D_j=3.57$, (Q) without shield at $\Phi=15^\circ$, $L/D_j=4.28$, $S/D_j=2.86$, $NPR=5$, at different relative times of (a) $102\mu s$, (b) $203\mu s$, (c) $304\mu s$, (d) $405\mu s$

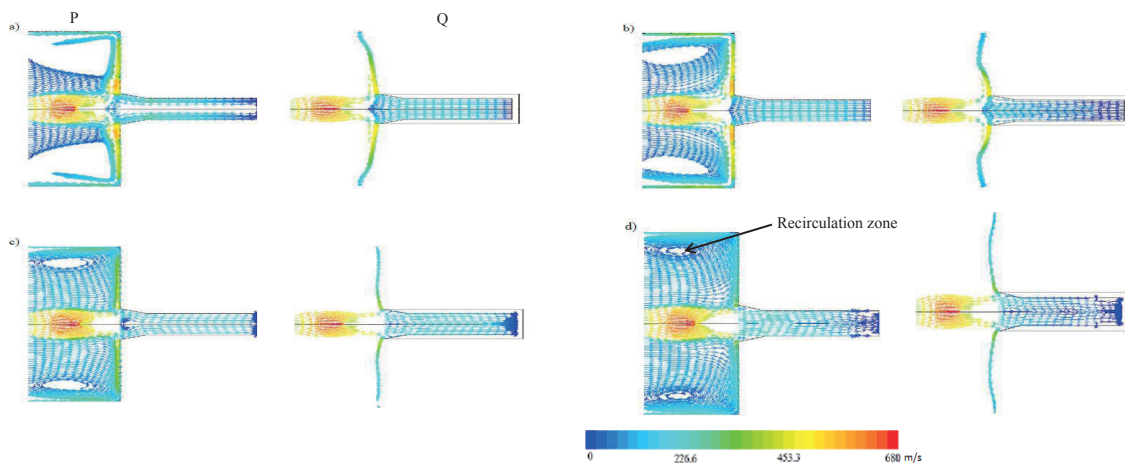


Fig. 8. Comparison of transient velocity vectors, (P) with $S/D_j=3.57$, (Q) without shield at $\Phi=15^\circ$, $L/D_j=4.28$, $S/D_j=2.86$, $NPR=5$, at different relative times of (a) $102\mu s$, (b) $203\mu s$, (c) $304\mu s$, (d) $405\mu s$

and un-shielded Hartmann whistles is of around 0.8. The velocity vectors of the shielded and un-shielded Hartmann whistles represent the beginning of the outflow phase and its subsequent increase in strength, as shown in Figs. 8 (a), 8 (b), 10 (a) and 10 (b). The beginning of the inflow phase is shown in Figs. 8 (c) and 10 (c) for both shielded and un-shielded whistles. A small recirculation zone was observed to form near the mouth of the shielded Hartmann whistle [Fig. 8 (c)]. The increase in the strength of the inflow phase leads to the beginning of the outflow phase and is further depicted in Figs. 8 (d) and 10 (d) for both shielded and un-shielded whistles. The formation of a strong recirculation zone was also observed near the shield wall, and it decreases in size as the height of the shield increases [Figs. 4 (d), 6 (d), 8 (d) and 10 (d)].

3.1.2 Comparison of the mass flow rate variations at the cavity inlet in the shielded and un-shielded Hartmann whistles

The variation in the mass flow rate according to the time at the cavity inlet for the shielded ($S/D_j=2.14, 2.43$) and un-shielded (WS) Hartmann whistles is shown in Fig.11 (a). The mass flow rate of the un-shielded Hartmann whistle (WS) exhibited sinusoidal behavior while a non-sinusoidal behavior was observed for the shielded whistles. The sinusoidal behavior of the mass flow rate in the un-shielded Hartmann whistle indicates that the cavity primarily operates in a jet regurgitant mode with a large spill-over around the mouth, and the shielded whistles exhibit a non-sinusoidal pattern of the mass flow rate without spill-over from the cavity mouth. The maximum mass flow entering

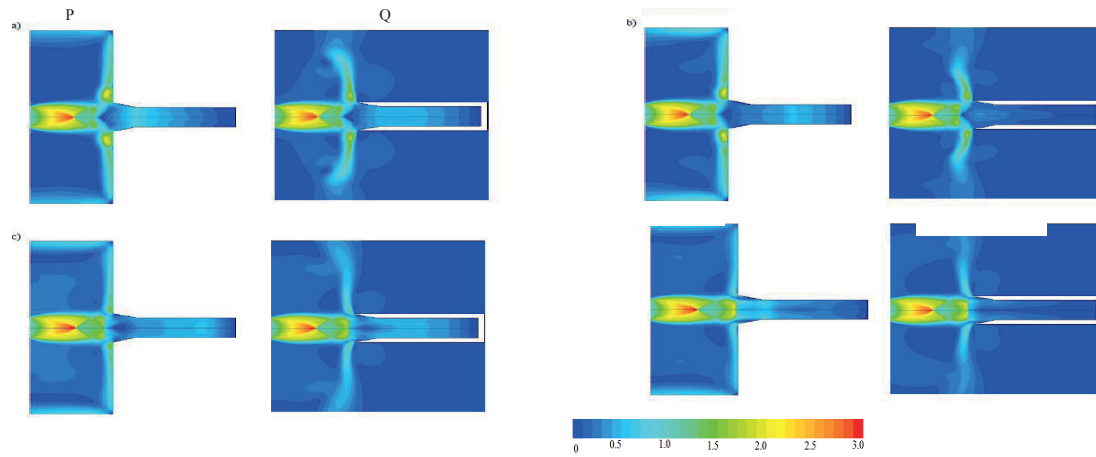


Fig. 9. Comparison of Mach number contours, (P) with $S/D_j=4.28$, (Q) without shield at $\Phi=15^\circ$, $L/D_j=4.28$, $S/D_j=2.86$, $NPR=5$, at different relative times of (a) $102\mu s$, (b) $203\mu s$, (c) $304\mu s$, (d) $405\mu s$

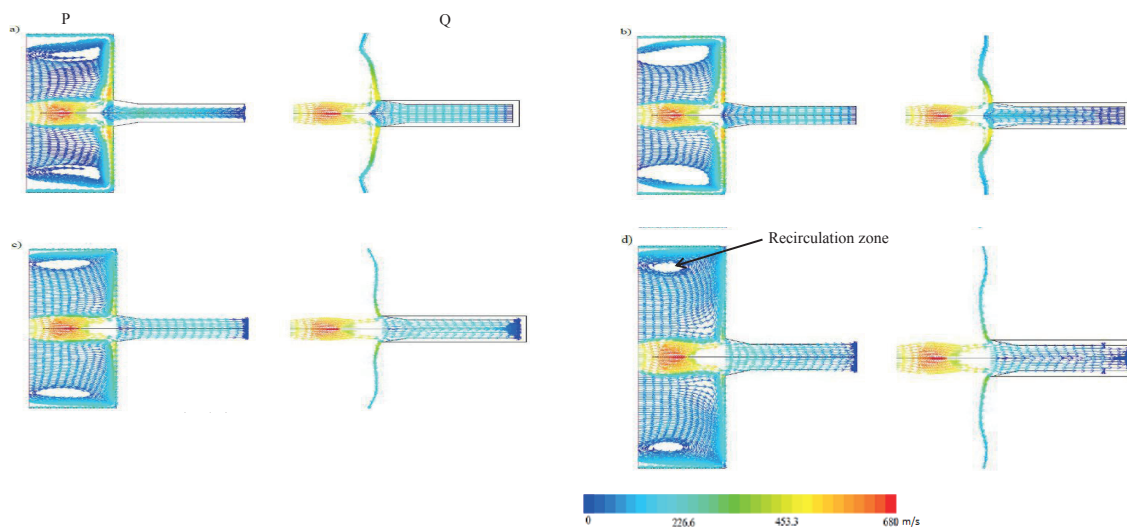


Fig. 10. Comparison of transient velocity vectors, (P) with $S/D_j=4.28$, (Q) without shield at $\Phi=15^\circ$, $L/D_j=4.28$, $S/D_j=2.86$, $NPR=5$, at different relative times of (a) $102\mu s$, (b) $203\mu s$, (c) $304\mu s$, (d) $405\mu s$

into the cavity of the 17 mm ($S/D_j=2.43$) shielded whistle was higher, and that for the 15 mm ($S/D_j=2.14$) shielded whistle was lower relative to the un-shielded whistles even though they follow the common trend for oscillatory behavior over time [Fig. 11 (a)]. Also, the magnitude of the maximum mass flow exiting the cavity in the 15 mm ($S/D_j=2.14$) shielded whistle is much lower than that of the un-shielded whistle while the maximum magnitude of the mass flow for the 17 mm ($S/D_j=2.43$) shielded whistle and the un-shielded is almost the same. Thus, the height of the shield is clearly shown to have a significant role in modifying the flow/shock oscillations near the mouth of the whistles. The mass flow rate variations for different shield heights, such as 20, 25 and 30 mm ($S/D_j = 2.86, 3.57$ and 4.28) are compared in Fig. 11 (b). The mass flow rate pattern in all shielded cases [Fig. 11 (b)] is observed to follow a stepped pattern, thus keeping its magnitude almost the same at around 0.03 kg/s. Although the shielded whistles also exhibit jet regurgitation like the un-shielded whistle, the presence of the shield can be concluded to exhibit a flow that moves toward the shield, thus completely eliminating

the flow diversion around the cavity mouth, as seen in the un-shielded whistle. The absence of a spill-over around the cavity mouth in the shielded whistle could significantly modify the flow/shock oscillations near its vicinity as well as the jet regurgitant phases, thus giving rise to the non-sinusoidal behavior of the mass flow at the cavity inlet.

3.1.3 Comparison of the variations in the axial velocity for the shielded and un-shielded Hartmann whistles

Figure 12 (a) shows a comparison of the variation in the axial velocity over time with $d/D_j=5.72$ from the nozzle exit along the chamfer for both the un-shielded and shielded whistles. The negative velocities are shown in Fig. 12 (a) for both the un-shielded and the shielded whistles and represent the reverse flow. The magnitude of the axial velocity is observed to be higher in the un-shielded whistles as compared to the shielded whistles ($S/D_j=2.14$ and 2.43). Also the magnitude of the axial velocity is shown to increase with the decrease in the shield height from $S/D_j=2.43$ to 2.14 [Fig. 12 (a)]. Thus, a faster flow is clearly observed to exit the un-shielded cavity than in the shielded ones. The variation

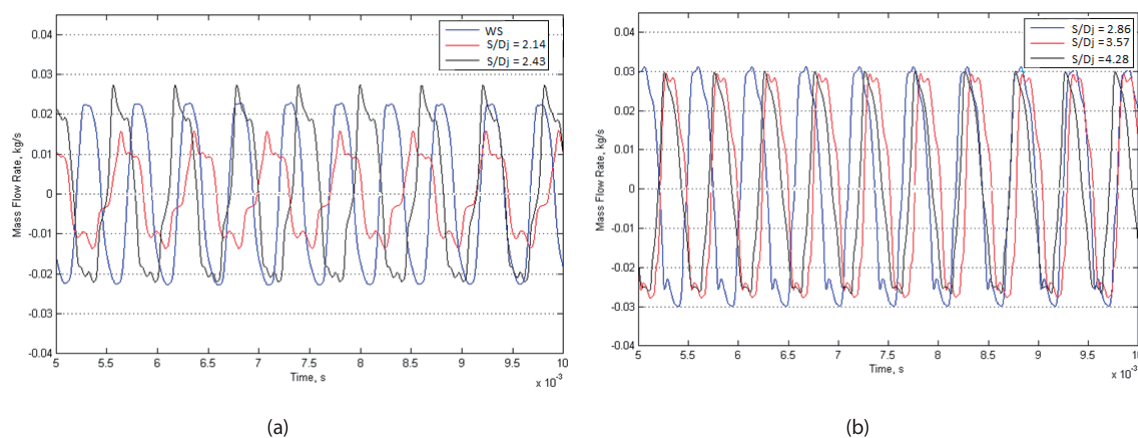


Fig. 11. Variation of mass flow rate with time at the cavity inlet for a) WS, $S/D_j=2.14$ and 2.43 b) $S/D_j=2.86, 3.57$ and 4.28

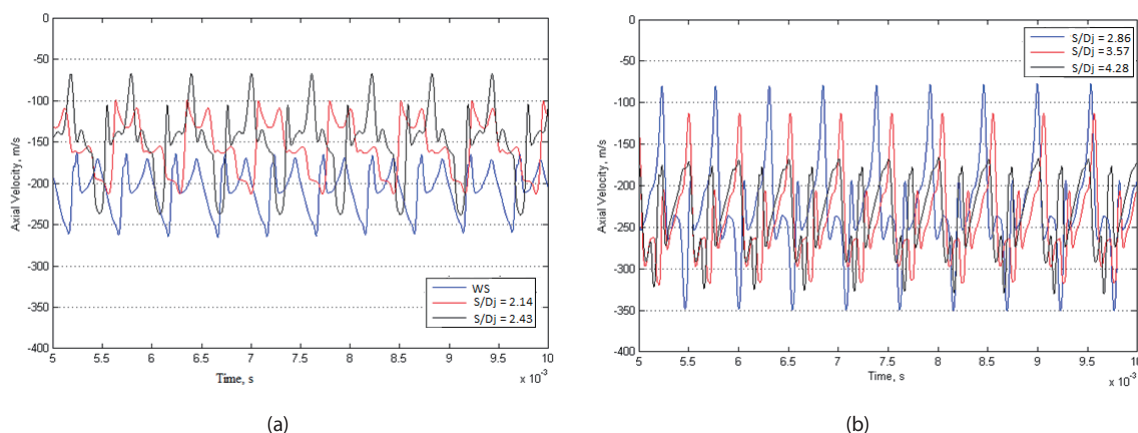


Fig. 12. Variation of axial velocity with time at $d/D_j=5.72$ from the nozzle exit along the chamfer for a) WS, $S/D_j=2.14$ and 2.43 b) $S/D_j=2.86, 3.57$ and 4.28

in the axial velocity for the 20 mm, 25 mm and 30 mm shielded cavities ($S/D_j=2.86, 3.57$ and 4.28) are shown in Fig. 12 (b). Among these shielded whistles, the magnitude of the axial velocity is observed to reach a maximum value for a large shield height of 30 mm ($S/D_j=4.28$). The cavity with a shield height of 30 mm [Fig. 12 (b)] behaves in a manner similar to that of the un-shielded ones [Fig. 12 (a)], thereby providing a faster flow reversal. Fig. 13 (a) provides a comparison of the variations in the axial velocity with time at a d/D_j value of 6.52 from the nozzle exit for both un-shielded and shielded whistles. The magnitude of the maximum inflow velocity is of around 100 m/s for a 17 mm ($S/D_j=2.43$) shielded whistle but decreases for the shield height of 15 mm ($S/D_j=2.14$) where the magnitude of the maximum inflow velocity is reduced to around 40 m/s and remains at around 75 m/s for the un-shielded whistle. Thus, the height of the shield is shown to play a crucial role in modifying the axial velocity. A comparison of the variation in the axial velocity of the 20 mm, 25 mm and 30 mm shielded cavities ($S/D_j=2.86, 3.57$ and 4.28) is shown in Fig. 13 (b). The magnitude of maximum inflow axial velocity is

of around 170 m/s for both the 20 and 25 mm ($S/D_j=2.86$ and 3.57) shielded whistles and is around 100 m/s for the 30 mm ($S/D_j=4.28$) shielded whistle. Thus, the effect of the shield height is further demonstrated to affect the axial velocity in the whistles. The variations in the axial velocity with time at a higher d/D_j value of 7.32 from the nozzle exit are shown in Fig. 14 (a) for both un-shielded and shielded whistles. Fig. 14 (a) shows features similar to those of Fig. 13 (a), with an increase in magnitude of the maximum velocity to around 220 m/s and 100 m/s for the 17 mm and 15 mm shielded whistles ($S/D_j=2.43$ and 2.14) and around 200 m/s for the un-shielded whistle. The comparisons of the axial velocity for various shield heights of 20 mm, 25 mm and 30 mm ($S/D_j=2.86, 3.57$ and 4.28) shown in Fig. 14 (b) indicate that the inflow velocity reached a peak value of around 280 m/s for a 25 mm shield height while the order of magnitude for the 20 mm and 30 mm shielded cases was almost the same. In general, the magnitude of the axial velocities in the un-shielded and shielded whistles is seen to not be comparable even though they exhibit oscillating behavior. The oscillating patterns of the axial velocities are also seen

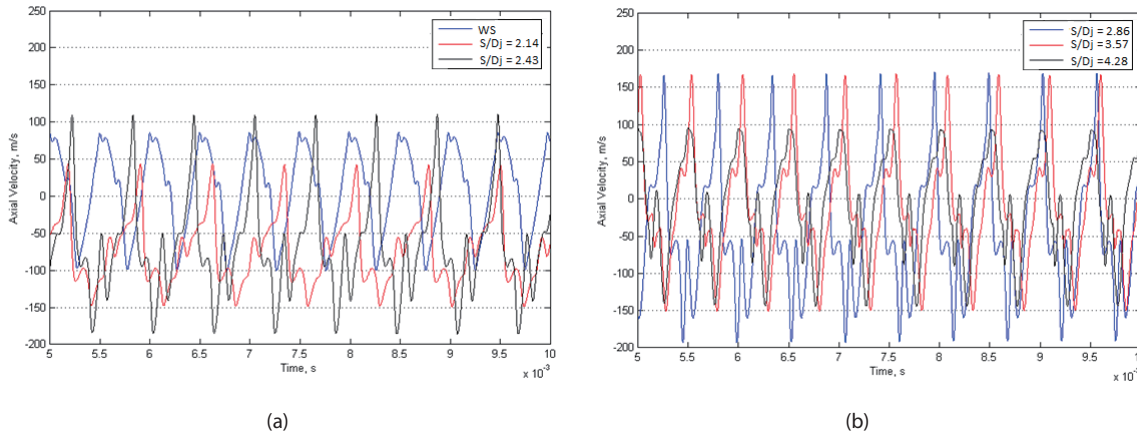


Fig. 13. Variation of axial velocity with time at $d/D_j=6.52$ from the nozzle exit along the chamfer for a) WS, $S/D_j=2.14$ and 2.43 b) $S/D_j=2.86, 3.57$ and 4.28

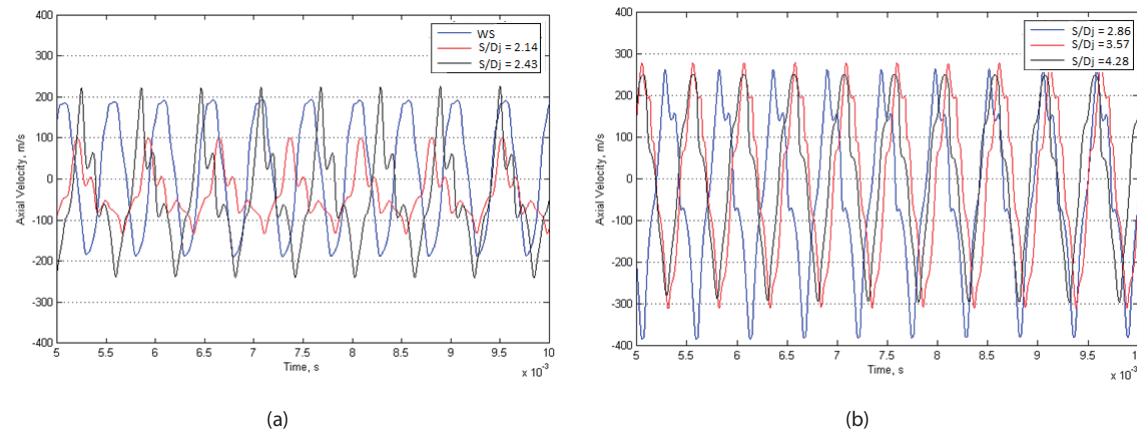


Fig. 14. Variation of axial velocity with time at $d/D_j=7.32$ from the nozzle exit along the chamfer for a) WS, $S/D_j=2.14$ and 2.43 b) $S/D_j=2.86, 3.57$ and 4.28

to be different for each case. This further demonstrates the effect of the shield in modifying the flow/shock oscillation features near the cavity mouth, thus giving rise to different axial velocity patterns. The axial velocity variations are compared in Fig. 15 (a) for un-shielded and shielded whistles at location P (10, 10) as shown in Fig. 1 (b). The 17 mm and 15 mm shielded whistle is observed to have large and small amplitude oscillations when compared to the un-shielded Hartmann whistle. The magnitude of the maximum axial velocity in the 17 and 15 mm shielded whistles is of 100 m/s and 20 m/s while that of the un-shielded whistle is of 50 m/s. The variation in the axial velocities at larger shield heights of 20 mm, 25 mm and 30 mm is shown in Fig. 15 (b). The magnitude of the maximum velocity (~150 m/s, 110 m/s, 70 m/s) is observed to decrease as the shield height increases from 20 mm to 30 mm. In general, the height of the shield can be concluded to be a crucial parameter that significantly influences the magnitude of the axial velocities as a result of the modification imparted to the flow/shock oscillations near the cavity mouth.

3.1.4 Comparison of the variations in the static pressure in shielded and un-shielded Hartmann whistles

Figure 16 (a) shows a comparison of the static pressure variations over time for both un-shielded and shielded whistles at $d/D_j=5.72$ from the nozzle exit. The un-shielded whistle is seen to possess higher static pressure oscillations relative to the shielded whistles. A comparison of the static pressure variations at $d/D_j=5.72$ for different shield heights to jet diameter ratios, $S/D_j=2.86, 3.57$ and 4.28 , as shown in Fig. 16 (b), reveals that the increase in the shield height causes a decrease in the static pressure. Fig. 17 (a) shows a comparison of the variations in the static pressure over time at $d/D_j=6.52$ from the nozzle exit for un-shielded and shielded whistles ($S/D_j=2.14$ and 2.43), and it is revealed to be higher for the shielded whistle with $S/D_j=2.43$ and to be lower for the un-shielded whistle while the static pressure of the shielded whistle with an S/D_j of 2.14 oscillates between them. A comparison of the variations in static pressure at $d/D_j=6.52$ for different shield height to jet diameter ratios ($S/D_j=2.86, 3.57$ and 4.28), as shown in Fig. 17 (b), also

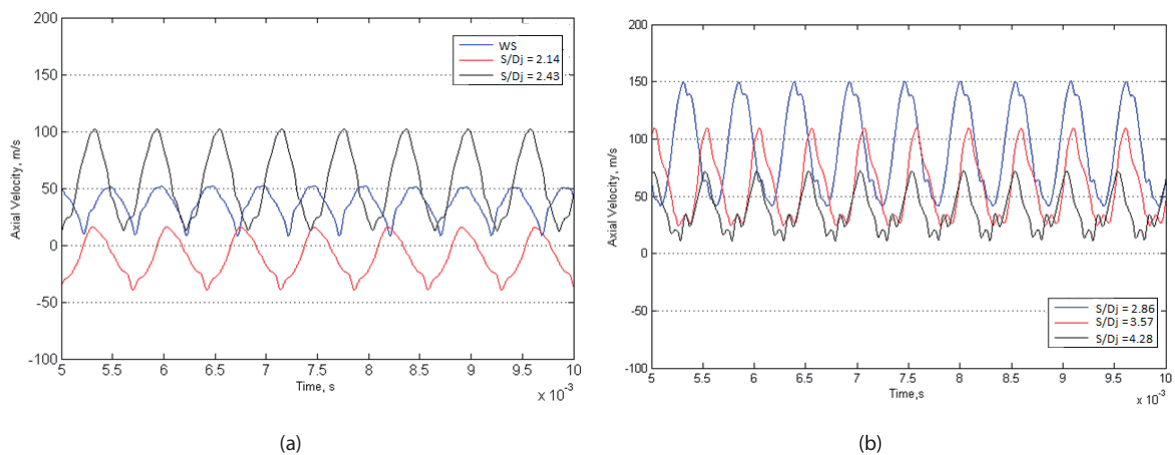


Fig. 15. Variation of axial velocity with time at P (10, 10) for a) WS, $S/D_j=2.14$ and 2.43 b) $S/D_j=2.86, 3.57$ and 4.28

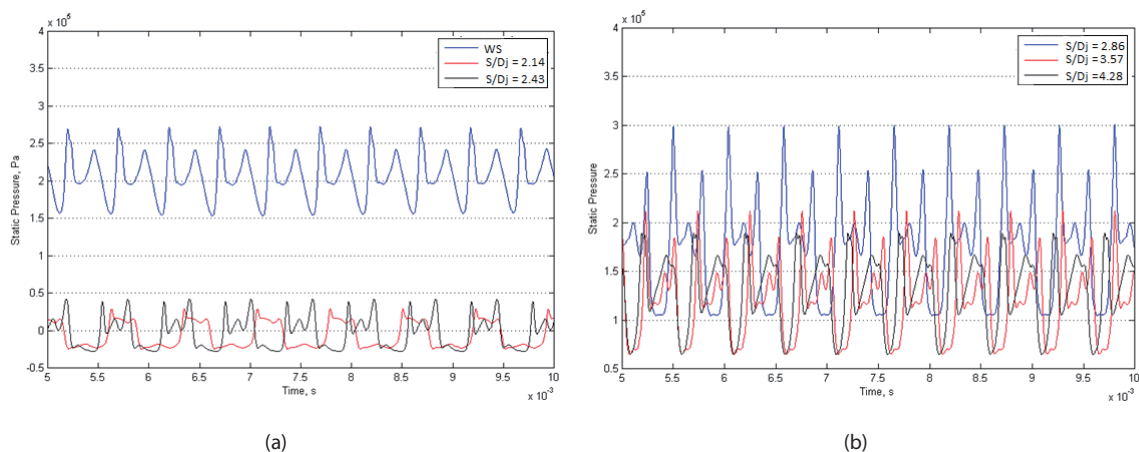


Fig. 16. Variation of static pressure with time at $d/D_j=5.72$ from the nozzle exit along the chamfer for a) WS, $S/D_j=2.14$ and 2.43 b) $S/D_j=2.86, 3.57$ and 4.28

follows similar behavior to that mentioned in Fig. 16 (b) above with different oscillation magnitudes. A comparison of the variation in static pressure variations at a higher d/D_j value of 7.32 for the un-shielded whistle to that of the shielded whistles [Fig. 18 (a)] with S/D_j 2.14 and 2.43 as well as for different shield heights of 20 mm, 25 mm and 30 [$S/D_j=2.86, 3.57$ and 4.28 ; Fig. 18 (b)] also exhibited behavior similar to that mentioned above in Figs. 17 (a) and 17 (b) with oscillations of different magnitudes. The variations in the static pressure for the un-shielded and the shielded whistles are compared in Fig. 19 (a) at location P (10, 10), as shown in Fig. 1 (b). The static pressure of the un-shielded whistle and the 15 mm shielded whistle ($S/D_j=2.14$) are observed to oscillate with high and low amplitudes while the 17 mm shielded whistle ($S/D_j=2.43$) oscillates between them. Furthermore, a comparison of the variations in the static pressure among whistles with a different shield height to jet diameter ratio [Fig. 19 (b)] shows that they follow different oscillatory patterns even though the maximum

magnitudes of their static pressure oscillations were almost similar in all cases.

4. Conclusions

Detailed numerical studies were conducted to understand the effect of various shield heights on the flow characteristics of a Hartmann whistle, and the results were compared to those of an un-shielded whistle. The presence of shield was seen to have a significant influence on the oscillation frequency. The whistle without a shield generates a frequency of 2.02 kHz, while that for the whistles with various shield heights varies between 1.4 kHz to 1.92 kHz, depending on the shield heights. A comparison of the Mach number contours and transient velocity vectors of the shielded Hartmann whistles to those of the un-shielded whistles with the same set of parameters and relative time instances showed that

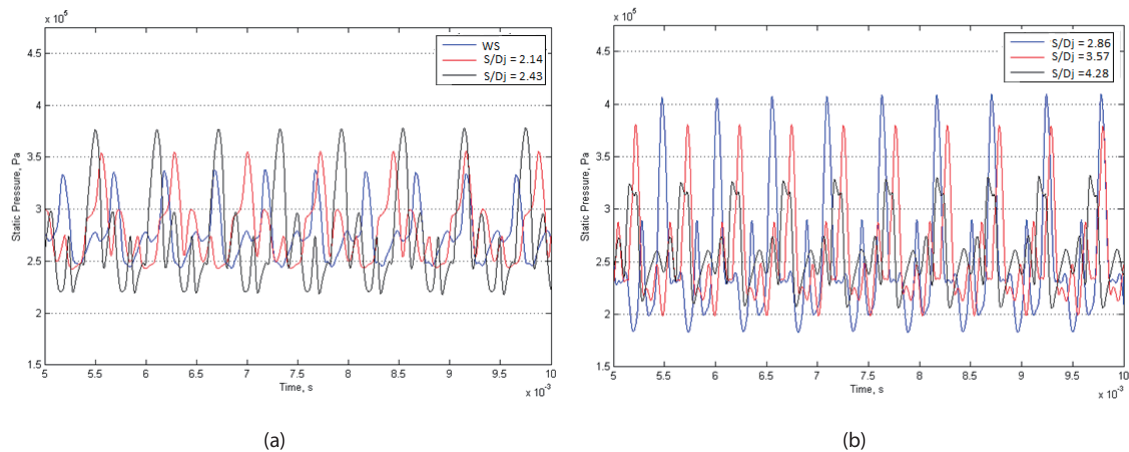


Fig. 17. Variation of static pressure with time at $d/D_j=6.52$ from the nozzle exit along the chamfer for a) WS, $S/D_j=2.14$ and 2.43 b) $S/D_j=2.86, 3.57$ and 4.28

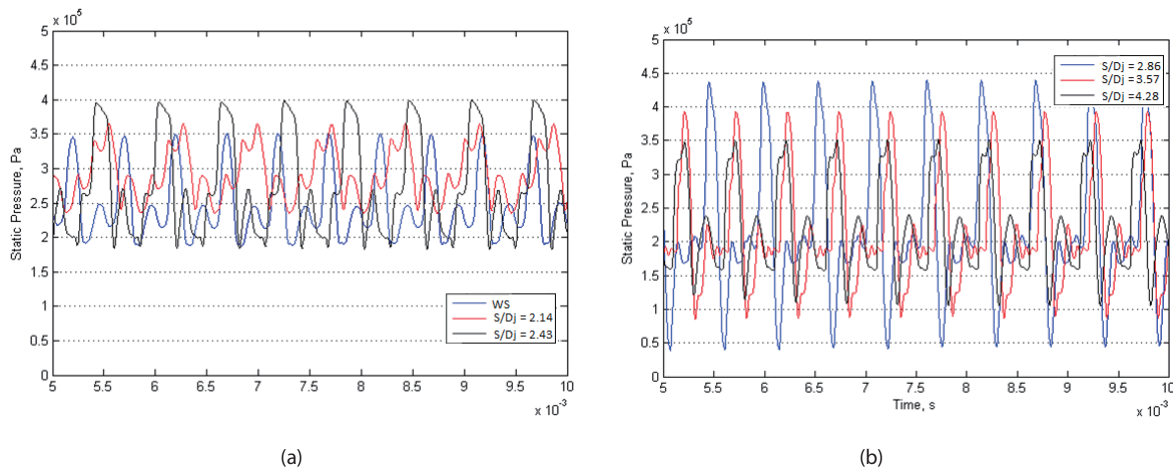


Fig. 18. Variation of static pressure with time at $d/D_j=7.32$ from the nozzle exit along the chamfer a) WS, $S/D_j=2.14$ and 2.43 b) $S/D_j=2.86, 3.57$ and 4.28

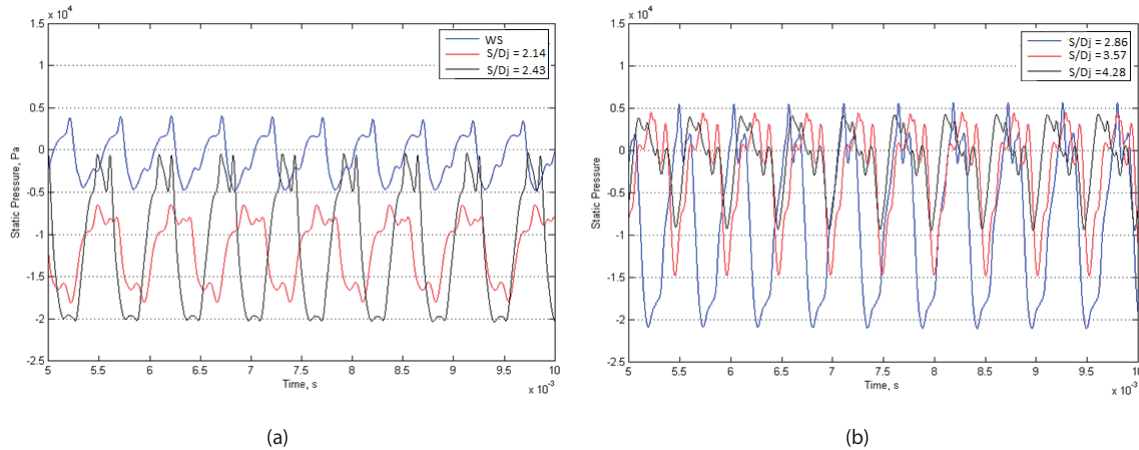


Fig. 19. Variation of static pressure with time at P (10,10) for a) WS, $S/D_j=2.14$ and 2.43 b) $S/D_j=2.86$, 3.57 and 4.28

the presence of the shield causes the jet to stick to the shield without causing any flow diversion around the cavity mouth, thus maintaining the shock oscillation as seen in the un-shielded Hartmann whistle. The velocity vectors depict jet regurgitation in the shielded Hartmann whistles that represents inflow and outflow phases as in un-shielded whistles with different jet regurgitant phases (i.e., inflow, outflow-phases) with the same relative time durations. The mass flow rate over time at the cavity inlet for the un-shielded whistle exhibits a sinusoidal behavior while a non-sinusoidal behavior can be observed for shielded whistles. The sinusoidal behavior of the mass flow rate for the un-shielded Hartmann whistle indicates jet regurgitation as the primary mode of operation with a large flow diversion around the mouth while mass flow rate exhibits a non-sinusoidal behavior in the shielded whistle, indicating that the jet regurgitation mode is not significant in this case. The magnitudes of the axial velocities in the un-shielded and the shielded whistles are not comparable even though they exhibit an oscillatory behavior. The pattern of the axial velocity oscillations is also seen to be different for each case. Thus, this paper sufficiently demonstrates the effect of the shield in modifying the flow/shock oscillations in the vicinity of the cavity mouth.

This paper provides a detailed numerical investigation of the effect of the shield height in terms of the modifications of flow characteristics, including flow/shock oscillations near the cavity mouth, operating modes of the Hartmann whistle, etc. Their behavior is compared to that of un-shielded whistles, and for a very large shield height (\sim infinity), the cavity may behave as an un-shielded one with a modified regurgitant phase without spill-over around the cavity mouth, which thus forms the main focus of this paper.

References

- [1] Hartmann, J. (1919) Om en ny metode til frembringelse af lydsvinginger. *DanMat Fys Medd*, 1:13.
- [2] K.S. Chang, K.H. Kim, and J. Iwamoto, "A study on the Hartmann Sprenger tube flow driven by a sonic jet", *International Journal of Turbo and Jet Engines*, Vol. 13, 1996, pp.173-182.
- [3] S.M. Chang, and S. Lee, "On the jet regurgitant mode of a resonant tube", *Journal of Sound and Vibration*, Vol. 246, No.4, 2001, pp. 567-581.
- [4] A. Hamed, K. Das, and D. Basu, "Characterization of powered resonance tube for high frequency excitation", *Proceedings of FEDSM'03 4TH ASME- JSME Joint Fluids Engineering Conference Honolulu*, FEDSM 2003-45472, Hawaii, USA, 2003.
- [5] E. Brun, and R.M.G. Boucher, "Research on the acoustic air-jet generator: a new development", *Journal of the Acoustical Society of America*, Vol. 29, No. 5, 1957, pp.573-583.
- [6] G. Raman, S. Khanafseh, A.B. Cain, and E. Kerschen, "Development of high bandwidth powered resonance tube actuators with feedback control", *Journal of Sound and Vibration*, Vol. 269, No. 3-5, 2004, pp. 1031-1062.
- [7] G. J. Sreejith, S. Narayanan, T. J. S. Jothi, and K. Srinivasan, "Studies on conical and cylindrical resonators", *Applied Acoustics*, Vol. 69, No. 12, 2008, pp. 1161-1175.
- [8] J.W. Gregory, and J.P. Sullivan, "Characterization of Hartmann tube flow with porous pressure sensitive paint", *Proceedings of the 33rd AIAA Fluid Dynamics Conference and Exhibit*, Orlando FL, 2003.
- [9] J. Kastner, and M. Samimy, "Development and characterization of Hartmann tube fluidic actuators for high-speed control", *American Institute of Aeronautics and Astronautics Journal*, Vol. 40, No. 10, 2002, pp. 1926-1934.
- [10] E. Brocher, C. Maresca, and M.H. Bournay, "Fluid

dynamics of the resonance tube”, *Journal of Fluid Mechanics*, Vol. 43, No. 2, 1970, pp. 369–384.

[11] S. Narayanan, K. Srinivasan, T. Sundararajan, and K. Ramamurthi, “Acoustic characteristics of chamfered Hartmann whistles”, *Journal of Sound and Vibration*, Vol. 330, 2011, pp. 2470-2496.

[12] G. Raman, and K. Srinivasan, “The powered resonance tube: from Hartmann’s discovery to current active flow control applications”, *Progress in Aerospace Sciences*, Vol. 45, 2009, pp. 97–123.

[13] P. R. Spalart, and S. R. Allmaras, “A One-equation Turbulence Model for Aerodynamic Flows”, *American Institute of Aeronautics and Astronautics*, 1992, AIAA-92- 0439.

[14] C.K.W. Tam, Jet noise generated by large-scale coherent motion, in: H.H. Hubbard (Ed.), *Aeroacoustics of Flight Vehicles, Theory and Practice*, vol. 1, Acoustical Society of America, Melville, 1995, pp. 1095.

[15] C.K.W. Tam, H.K. Tanna, “Shock associated noise of supersonic jets from convergent-divergent nozzles”, *Journal of Sound and Vibration*, Vol. 81, 1982, pp. 337–358.